Hindawi Publishing Corporation
Mathematical Problems in Engineering
Volume 2015, Article ID 918296, 18 pages
http://dx.doi.org/10.1155/2015/918296

Research Article

A High Power Density Integrated Charger for Electric Vehicles with Active Ripple Compensation

Liwen Pan[1,2] and Chengning Zhang[1]

[1] *School of Mechanical Engineering, Beijing Institute of Technology, Beijing 100081, China*
[2] *Department of Electrical and Electronic Engineering, University of Bristol, Bristol BS8 1TH, UK*

Correspondence should be addressed to Liwen Pan; panliwen2002@163.com

Received 1 August 2015; Revised 14 October 2015; Accepted 18 October 2015

Academic Editor: Xiaosong Hu

This paper suggests a high power density on-board integrated charger with active ripple compensation circuit for electric vehicles. To obtain a high power density and high efficiency, silicon carbide devices are reported to meet the requirement of high-switching-frequency operation. An integrated bidirectional converter is proposed to function as AC/DC battery charger and to transfer energy between battery pack and motor drive of the traction system. In addition, the conventional H-bridge circuit suffers from ripple power pulsating at second-order line frequency, and a scheme of active ripple compensation circuit has been explored to solve this second-order ripple problem, in which a pair of power switches shared traction mode, a ripple energy storage capacitor, and an energy transfer inductor. Simulation results in MATLAB/Simulink validated the eligibility of the proposed topology. The integrated charger can work as a 70 kW motor drive circuit or a converter with an active ripple compensation circuit for 3 kW charging the battery. The impact of the proposed topology and control strategy on the integrated charger power losses, efficiency, power density, and thermal performance has also been analysed and simulated.

1. Introduction

It is a significant strategy on a global scale to replace fossil fuels vehicles with electric vehicles (EVs) for protecting the environment and achieving energy sustainability [1]. EVs have gained wide attention from the past years as one of the effective solutions for environment deterioration and energy shortages. There are three barrier issues for gaining tremendous acceptance for EVs, which include the high cost and cycle life of batteries, the lock of charging infrastructure, and integrations of chargers. Integrated charger can avoid these problems by integrating with electric drive and battery charger. The main advantages of integrated charging methods are that the weight, volume, and cost are reduced. The configuration of a conventional EV is shown in Figure 1(a). However, the components in the traction circuit, like the inverter, are not used during the battery charging, so it is possible to use it in the charger circuit. The typical structure of an integrated charger is shown in Figure 1(b).

Several organizations such as Society of Automotive Engineers (SAE) have supplied the utility interface for EV conductive charge coupler. As shown in Table 1, most EV charging can be installed at home where the EV can be connected with a convenience household outlet for Level 1 charging. Level 1 charging requires a 120 V or 230 V outlet. Usually single-phase converter is used for that solution. A bidirectional on-board charger needs a highly efficient AC-DC converter that boasts a high power density and fits the limited space and weight requirements.

Battery charger plays an important role in the development of EVs. In most of traditional distributed EVs electrical systems, motor drive circuit and battery charger circuit are separate, so two independent circuits are needed. However, the integrated charger supplies flexibility for layout space, weight, and cost for EVs to obtain high efficiency and higher power density [2–4]. Different types of integrated charger topologies design have been reported and explained in previous papers [5–8]. Similar topologies are introduced in [9–11], without further power losses analysis, efficiency, and thermal stress issues. Besides these, an integrated charger for plug-in electric vehicles based on a special interior permanent magnet motor is introduced. An interior permanent magnet

Table 1: Charging power levels (based in part on [37]).

Power level types	Level 1	Level 2	Level 3
Supply voltage	120 V_{AC} (US) 230 V_{AC} (EU)	240 V_{AC} (US) 400 V_{AC} (EU)	208–600 V_{AC} or V_{DC}
Power level	≤3.7 kW	3.7–22 kW	>50 kW
Charging time	11–36 hours	1–6 hours	0.2–1 hours
Charger location	On-board	On-board	Off-board
	1-phase	1-phase or 3-phase	3-phase
Energy supply interface	Convenience household outlet	Dedicated EV supply equipment	Dedicated EV supply equipment
Battery capacity	16–50 kWh	16–50 kWh	16–50 kWh

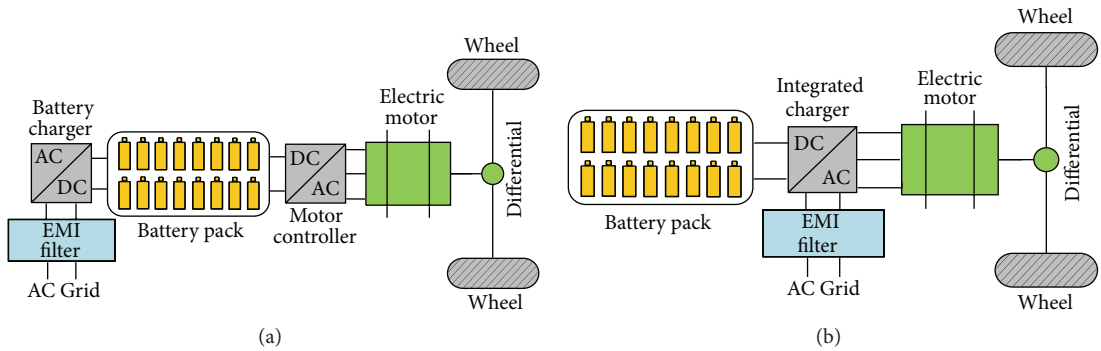

Figure 1: Configuration of electric vehicle: (a) configuration of a conventional electric vehicle and (b) configuration of an integrated charger electric vehicle.

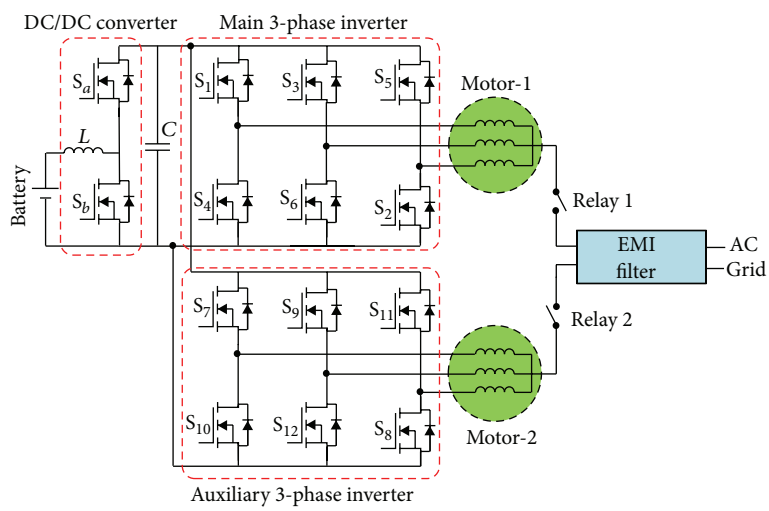

Figure 2: Integrated charger with two motors and two inverters.

synchronous is designed with a special winding configuration for traction mode and charging mode [12]. For integrated fast battery charger, a fast on-board battery charger using the motor like filter and the same converter for traction and charging mode is presented as well [13].

The topology as shown in Figure 2 is used for plug-in hybrid vehicles. The two three-phase AC motors are used as inductors for the converter with the neutral points connected to the grid. In traction mode, motor-1 delivers energy as a traction motor while motor-2 is used to charge the battery. In the charging mode, both of the motors and converters operate as AC-DC boost converter to charge the battery [14]. However, this topology needs two motors or special double winding motor and converters to make the system complex.

A permanent magnet nonisolated integrated charger topology is proposed in Figure 3. The AC three-phase grid is connected to each winding neutral point of the motor. The magnetic motive force is cancelled on the stator. The magnetic decoupling between the stator and the rotor prevent the rotor from vibrating during charging mode. No rotation

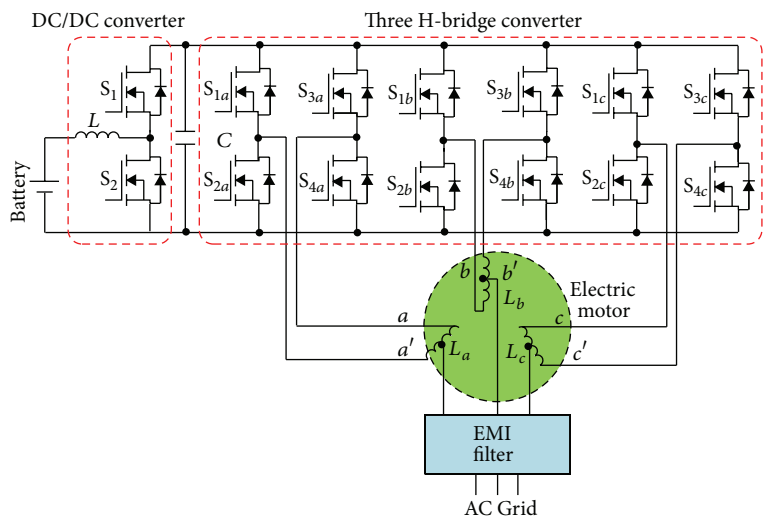

Figure 3: Integrated charger topology connecting to PM motor winding as filter.

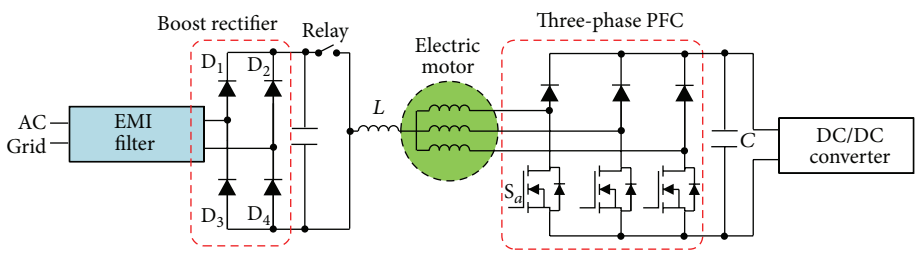

Figure 4: Integrated charger with three-phase PFC.

is produced during the charging mode [15]. However, this topology needs to use PMSM windings as coupling filter. It is not proper to use if the motor winding inductance is less than the filter requirement.

An integrated charger is shown in Figure 4. An interior permanent magnet motor drive circuit is operated as a three-phase PFC circuit during charging mode. No additional filter is needed except for electric motor windings. The disadvantage of this topology is a single-phase diode bridge rectifier that is used as the battery charger [16]. Therefore, a large buck capacitor is needed to divert the ripple power from DC-link. The aluminium electrolytic capacitor offers low cost and a high energy density. However, this type of capacitors has a short lifetime which is unacceptable in EVs application. Film capacitor is more reliable than electrolytic capacitor for electric vehicles, which results in low power density. This inevitably leads to an increased system cost and degraded energy efficiency. Various active ripple compensation methods are proposed to absorb the low-frequency ripple energy. An active filter is used to divert the ripple power from the DC-link in existing methods [17].

High efficiency and high power density are expected to achieve for integrated charger design. The converter power density is evaluated by measuring the volume of power modules, cooling system, line inductor, and DC-link capacitor [18] as shown in Figure 5. In addition, the power density is required to constraint on space and weight of the overall

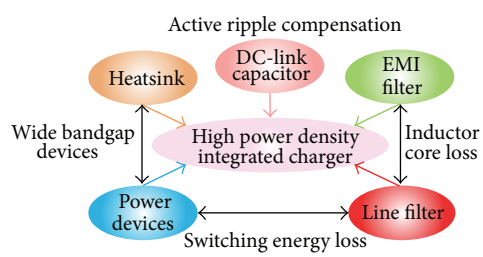

Figure 5: High power density converter design.

system. High power density system is considered by the use of new materials switching devices, increase in integrated levels, and design of innovative circuit to reduce the size of DC-link capacitor in this paper.

Conventional converter based on silicon (Si) devices typically operate at lower frequency contrasting with silicon carbide (SiC) MOSFETs. SiC switching devices are developing rapidly in the market in recent years. This supplies opportunities for smaller converter optimization design. High switching frequency can directly affect the size of converter's heatsink, DC-link capacitor, line filter, and EMI filter [19]. In order to optimise the integrated charger efficiency and power density, the SiC switching devices are used as the switches in this paper.

In this paper, a concept of high power density integrated charger for electric vehicles with active ripple compensation

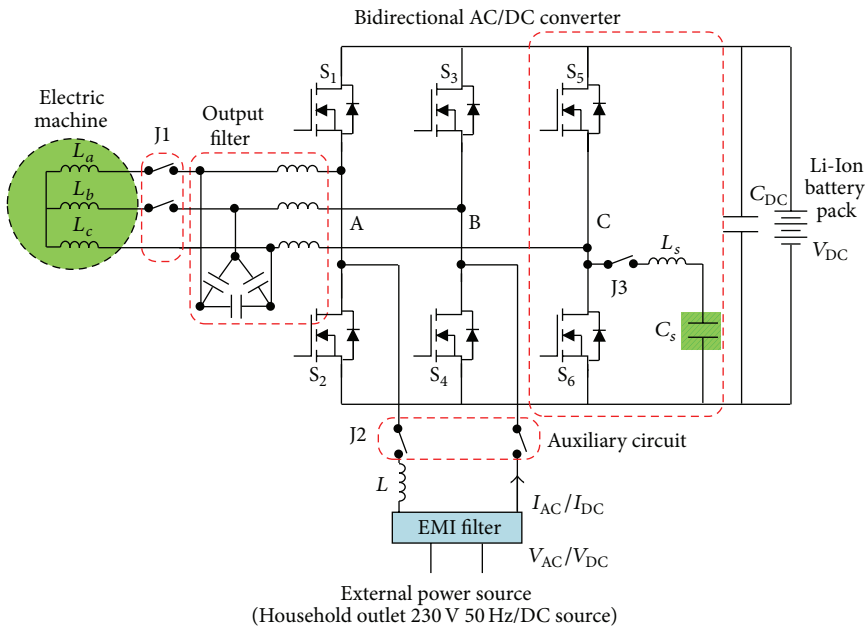

Figure 6: Topology of the integrated charger for electric vehicles.

is reported. The paper is organized as follows: the existing on-board battery charger in EV/HEV applications is introduced in Section 1. The topology of a high power density integrated charger with active ripple compensation is explained in Section 2. The design criteria of circuit components are described in Section 3. Section 4 presents an active ripple energy storage control method. Moreover, the main energy storage component inductor method and capacitor method are theoretically analysed and simulated. A capacitor auxiliary energy storage circuit is designed in details. The simulation results in Section 5 show that the design and control strategy meet the demand. The integrated charger system power losses and thermal performance are discussed in Section 5. Finally, the conclusion is given in Section 6.

2. Concept of Integrated Charger with Active Ripple Compensation

The concept of a high power density integrated charger for electric vehicles with active ripple compensation is illustrated in Figure 6. The switches and passive components are shared and multiused for traction mode and charging mode. In traction mode, the grid is not connected to the converter by turning off the relays between grid and converter. The grid current flows in the battery through the H-bridge converter during the battery charging. By this way, the electrical motor cannot rotate, because the relays beside the motor are open in the driving mode [20].

2.1. Topology. A schematic of the proposed integrated charger with active ripple compensation converter is shown in Figure 6. It includes an electric motor, a battery pack, an LC output filter, a DC-link capacitor, and an active ripple reduction circuit. Relays are added to the circuit to achieve different operations modes [21]. The motor drive system can provide the required drive torque and battery charging in AC power and DC power operational modes. The DC power can be converted into AC power by a three-phase inverter to charge the battery. The H-bridge rectifier can support both AC and DC charging. The power flow between the motor, the battery, and power source is shown in Figure 7.

2.1.1. Motor Drive Modes. In the motor drive mode, relay J1 is switched on for propulsion, and relay J2 and relay J3 are open. The EV is operating at electric propelling mode, and its power flows from the battery pack to the motor. Figure 6 shows the conventional three-phase voltage-source converter structure. The three-phase rectifier circuit consists of three legs A, B, and C. The output of each leg depends on DC-link voltage and the switch status, and the output voltage is independent of the output load current since one of the two switches in a leg is always on at any instant. The DC voltage-source battery feeds the main rectifier circuit, a three-phase bridge. The DC voltage source is battery pack. Six switches are used in the main circuit. Each is composed of a SiC MOSFET and an antiparallel diode to provide bidirectional current flow and unidirectional voltage blocking capability. The converter works as a buck inverter for DC-to-AC power conversion.

2.1.2. AC Power Battery Charging Modes. The battery pack can be charged by the external power supply. When in the charging mode, the drive motor needs to be disengaged for safety purpose. Therefore, relay J1 keeps open to disconnect the three-phase windings in the motor. In addition, relays J2 and J3 are closed for charging. The battery pack can be charged by a low-voltage single-phase grid as a boost rectifier for AC-to-DC power conversion [22].

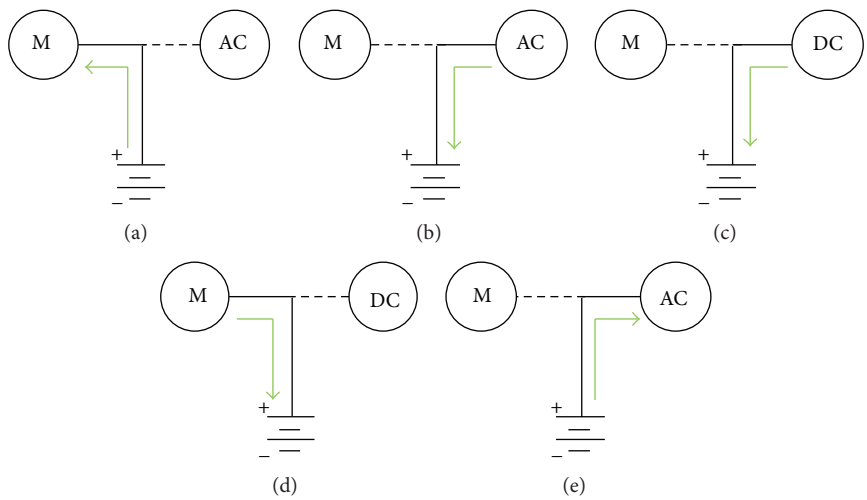

Figure 7: Power flow: (a) motor drive mods, (b) AC power charging, (c) DC power charging, (d) regenerative charging, and (e) vehicle-to-grid.

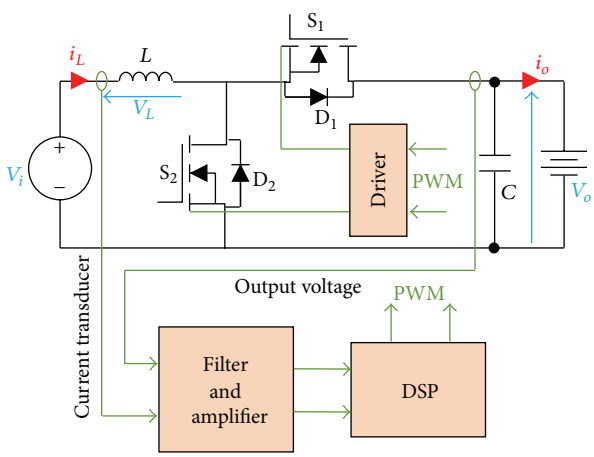

Figure 8: Boost DC/DC converter.

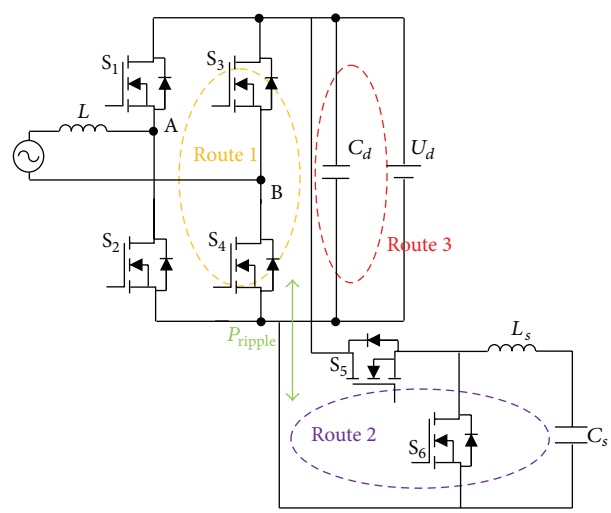

Figure 9: Active ripple compensation circuit.

2.1.3. DC Power Battery Charging Modes. The battery pack can be charged by low-voltage DC power, as shown in Figure 8. Boost operation from DC input voltage to the high-voltage battery pack of the EV is shown in Figures 10(a) and 10(b).

In this mode, S_2 works for PWM switching, and D_1 provides a free-wheeling path. Other switches and diodes S_1, D_2, S_3, and S_4 maintain the OFF state. The state of charge (SOC) should be regulated by measuring battery voltage and current.

2.1.4. Regenerative Braking. The proposed bidirectional converter is properly combined to select buck-and-boost modes among voltage sources. Regenerative charging uses buck operation from the high-voltage bus to the battery pack.

2.1.5. Vehicle-to-Grid (V2G). V2G is a modified version of EVs for the next generation to spark a revolution in the development of transportation and energy industries [23]. The V2G vehicles have capability of both charging from the grid and discharging to the grid intelligently that utilize bidirectional H-bridge converter properly.

2.1.6. Active Ripple Compensation Circuit. The grid voltage and current are sinusoidal, and twice the line frequency ripple will be generated on the DC-link, which is harmful to both sides of the converter. Especially when a battery connected on the DC-link, the pulsating power will lead to overheat. A relatively large DC-link capacitor is usually used to limit the ripple power, but it results in higher volume, weight, and cost for the integrated charger. To solve this second-order pulsating power, active ripple compensation methods have been explored in the paper.

The active ripple compensation circuit is composed of the active filter switches S_5 and S_6 which are shared with three-phase rectifier for motor drive circuit, an energy store capacitor, and an energy transfer inductor, as shown in Figure 9.

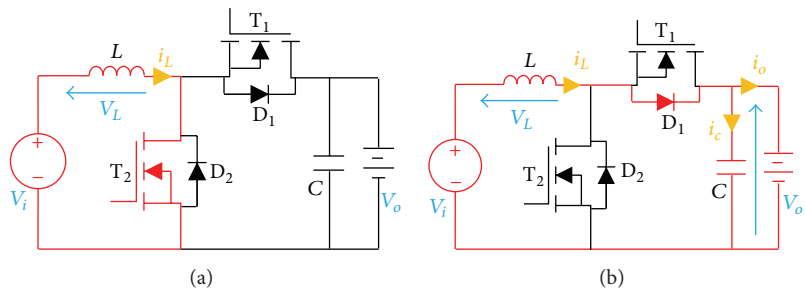

Figure 10: Boost converter circuit operating phases: (a) T_2 state-on, D_1 state-off, and (b) D_1 state-on, T_2 state-off.

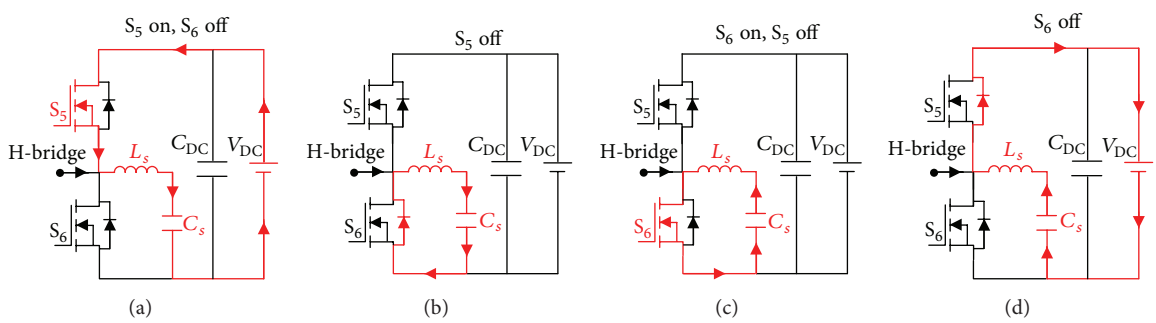

Figure 11: Equivalent circuit of active ripple compensation circuit for each stage of operation. ((a), (b)) Buck charging phase and ((c), (d)) boost discharging phase.

The C-phase accomplishes the DC side pulsating power at twice the grid frequency. The effectiveness of the active ripple compensation method is confirmed by simulation results. When switch S_5 turns on, the active ripple compensation circuit works as in buck phase. The capacitor and inductor are charged by DC bus. The inductor will release its energy to capacitor when the S_5 turns off. While switch S_6 is used to control the active ripple compensation circuit works as in boost phase. When the switch S_6 turns on, the capacitor releases its energy to inductor. When the switch S_6 turns off, the DC bus is charged by both of capacitor and inductor. A DC bus capacitor C_{DC} is still needed to filter the high frequency ripple power of the PWM rectifier output. In this case, C_{DC} is smaller than conventional method without the active ripple compensation storage circuit. The equivalent circuit of active ripple compensation circuit for each stage of operation is shown in Figure 11.

2.2. Instantaneous Power Balance Analysis. The grid-side supply voltage u_{AC} and current i_{AC} are assumed to be sinusoidal, the grid power supply can be written in (1), and the power of the input inductor can be expressed as (2):

$$\begin{aligned} P_{AC} &= u_{AC}(t) * i_{AC}(t) \\ &= \frac{1}{2}U_{AC}I_{AC}\cos\varphi - \frac{1}{2}U_{AC}I_{AC}\cos(2\omega t - \varphi), \end{aligned} \tag{1}$$

where U_{AC} and I_{AC} are the peak value of voltage and current, respectively, ω is the angular frequency, and φ is the angle between the grid supply voltage and current:

$$P_L = \omega L I_{AC}^2 \sin(\omega t - \varphi)\cos(\omega t - \varphi). \tag{2}$$

The input power of the single-phase converter after the input inductor can be determined by (1) and (2), where L is the inductance of input filter:

$$\begin{aligned} P_{in} = P_{AC} - P_L &= \frac{1}{2}U_{AC}I_{AC}\cos\varphi \\ &- \left(\frac{1}{2}U_{AC}I_{AC}\cos(2\omega t - \varphi)\right. \\ &\left. + \frac{1}{2}\omega L I_{AC}^2 \sin(2\omega t - 2\varphi)\right). \end{aligned} \tag{3}$$

As can be seen in (3), a constant power and twice the fundamental frequency 2ω power pulsating consist of the input power of the single-phase battery charging circuit. To ensure a low-frequency ripple in single-phase charger, a large DC capacitor is required which results in low power density. In order to avoid the second-order harmonic and minimize the size of DC capacitor, a DC ripple current reduction method on a single-phase PWM voltage-source rectifier has been investigated in [24]. Several active solutions have been explored to reduce the second-order ripple power, namely, inductive storage method and capacitive storage method. The active ripple compensation charging circuit is shown in Figure 12.

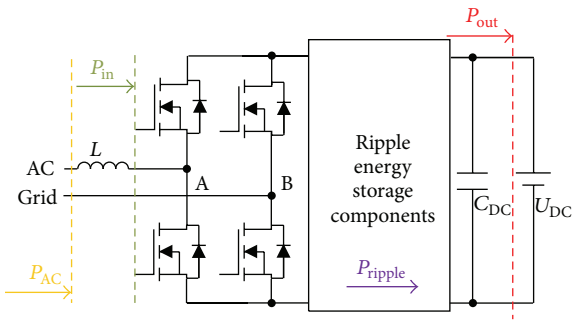

Figure 12: Active ripple compensation charging circuit.

A conventional H-bridge rectifier consists of phase-A and phase-B. The AC supply power is P_{AC} which can be expressed by AC source voltage multiplied AC source current. L is the input inductor which is used to keep a constant current flowing to the load throughout the complete cycle of the applied voltage. The input power of the H-bridge rectifier after the input inductor is P_{in}. It is known that there exists second-order harmonic power P_{ripple} on DC-link for H-phase rectifier. The constant power on DC-link can be expressed as P_{out}. Generally speaking, the basic approach behind the ripple reduction circuit involves storage of the ripple power into inductor or capacitor. The comparison between inductive storage method and capacitor method is discussed in Section 3.

3. Design Criteria of Circuit Components

3.1. Selection of Motor Drive Circuit Components. A buck converter with LC filter should be considered in the three-phase inverter to reduce the ripple. An LC filter is critical for AC motor drive application. The capacitors can be configured with a delta connection which has the benefit of smaller short circuit current. Capacitor and choke values are derived to optimize the two-level inverter output performance. The filter is assumed to filter out all the PWM switching harmonics. Damping is required to attenuate the resonance and the output impedance of the filter should be as small as possible across the frequency range. A series resonance occurs at the output filter resonant frequency f_0. Hence, the corner frequency is kept below the switching frequency. The result can be expressed as in

$$f_0 = \frac{\omega_0}{2\pi} = \frac{1}{2\pi\sqrt{LC}}, \tag{4}$$

where f_0 represents the corner frequency, for 10% attenuation of switching frequency harmonics. L and C are the inductance and capacitance, respectively. The key characteristics in the driving mode are shown in Table 2.

3.2. Selection of Battery Charging Circuit Components. A typical H-bridge connected with an active ripple compensation circuit works as battery charging converter. The A-phase and B-phase operate as conventional PWM. A large filter capacitor is connected on the DC side [25]. The required DC-link capacitance can be expressed as

$$C_{DC} \geq \frac{P_{avg}}{\omega_0 \cdot \Delta V \cdot V_{DC}}, \tag{5}$$

where ΔV is the amplitude of DC-link voltage ripple, for 2% allowable voltage ripple, C_{DC} is the value of DC-link capacitor, V_{DC} is the DC-link voltage, ω_0 is the AC-side circular frequency, and P_{avg} is the average power flowing into the converter. The complete parameters in battery charging mode are listed in Table 3.

Table 2: Key characteristics in the motor drive mode.

Items	Parameters
Rated output power P_{out}	70 kW
Switching frequency f_{sw}	10 kHz
Modulation index	0.9
Cooling method	Water cooling
DC-link voltage V_{DC}	320 V
Output LC filter inductance L	267 μH
Output LC filter capacitance C	10 μF

Table 3: Parameters in battery charging mode.

Items	Parameters
AC voltage source V_{AC} (RMS)	230 V
Line frequency f	50 Hz
Rated output power P_{out}	3 kW
Input inductor L_1	4.35 mH
DC-link capacitance C_{DC}	4665 μF
Switching frequency f_{sw}	20 kHz
DC-link voltage V_{DC}	320 V
Modulation index	0.9
Cooling method	Natural cooling

3.3. Selection of Ripple Energy Storage Circuit Components. The ripple energy generated by H-bridge can be determined in

$$\begin{aligned} E_r &= \frac{P_r}{\omega} \\ &= \frac{\sqrt{P_0^2 + \left[\left(2\omega L P_0^2 / U_s^2 \cos^2\varphi\right) - P_0\left(\sin\varphi / \cos\varphi\right)\right]^2}}{\omega}. \end{aligned} \tag{6}$$

Equation (6) shows the relationship between ripple energy, the angle of grid voltage, the output power, AC supply voltage, the AC supply frequency, and current and input inductor. The parameters of a 3 kW single-phase PWM rectifier are given in Table 3. The relationship between various and the ripple energy is plotted in Figures 13(a) and 13(b).

It can be observed that the phase inductor has an obvious influence on the ripple energy. The higher inductance results in a higher ripple energy. Meanwhile, the supply frequency has an obvious influence on the ripple energy as well.

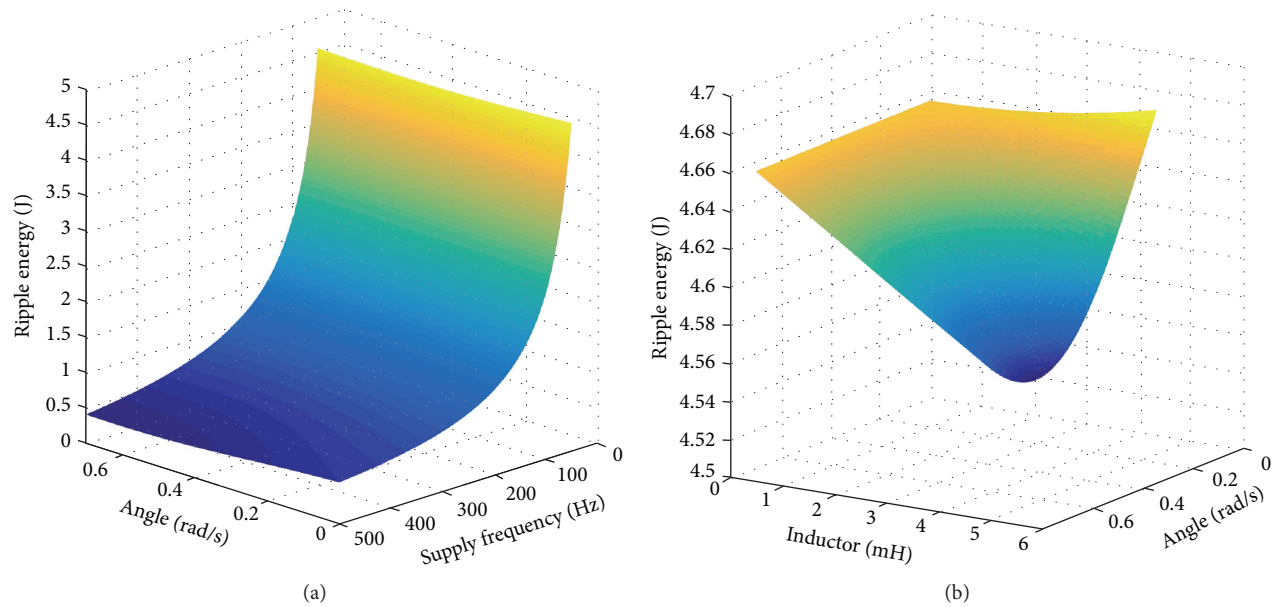

FIGURE 13: Ripple energy: (a) relationship between angle of the supply voltage and current and supply frequency and (b) relationship between angle of the supply voltage and current and inductor.

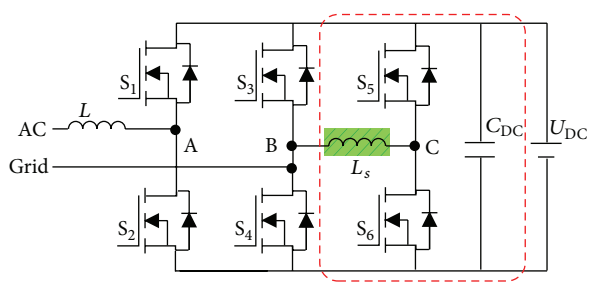

FIGURE 14: Circuit configuration.

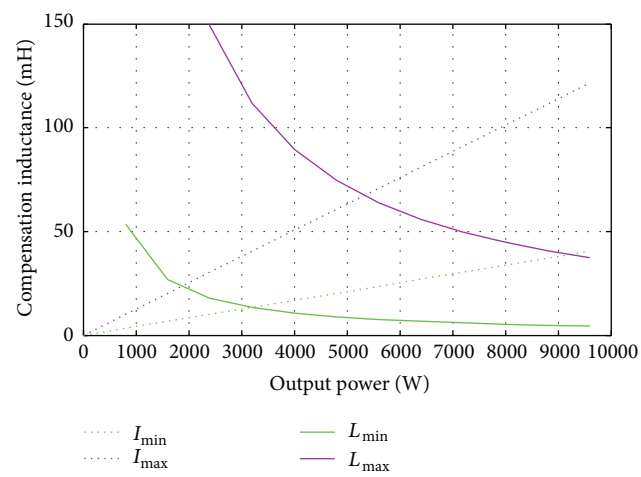

FIGURE 15: Compensation region of the inductor.

The lower supply frequency leads to a higher power pulsating. The reason can be expressed in (6). Figure 13(b) shows that there is a minimum of 4.67 J ripple energy for the 3 kW single-phase rectifier system.

3.4. Inductive Storage Method. Figure 14 shows the circuit configuration of inductive storage method. A conventional single-phase rectifier consists of A-phase leg, B-phase leg, input filter, and DC-link capacitor. An active ripple energy storage circuit consists of C-phase leg and a ripple energy storage inductor. One terminal of the storage inductor is connected to the midpoint of the C-phase leg switches (connection point of S_5 and S_6), while the other terminal is tied to B-phase leg of the H-bridge converter. The compensation inductance L used to store ripple energy should be selected depending on the output power P_{out}. A DC bus capacitor C_{DC} is still necessary to filter the high switching harmonic. The DC ripple energy flows into the inductor. The inductance can be selected in a wide rage when the inductor current is controlled properly. The maximum inductor current and the minimum inductor current are shown in

$$L_{max} = \frac{2I_{AC}V_{AC}}{I_{min}^2\omega}, \qquad L_{min} = \frac{\sqrt{2}V_{AC}}{2D\lambda f_{sw}I_{min}}, \tag{7}$$

where L_{max} is maximum inductance, L_{min} is minimum inductance, λ is modulation factor of the single-phase, and V_{AC} and I_{AC} are the grid voltage and grid current, respectively. And D is the ratio between peak ripple current and minimum ripple current. The compensation inductance and current region are shown in Figure 15. Higher switching frequency

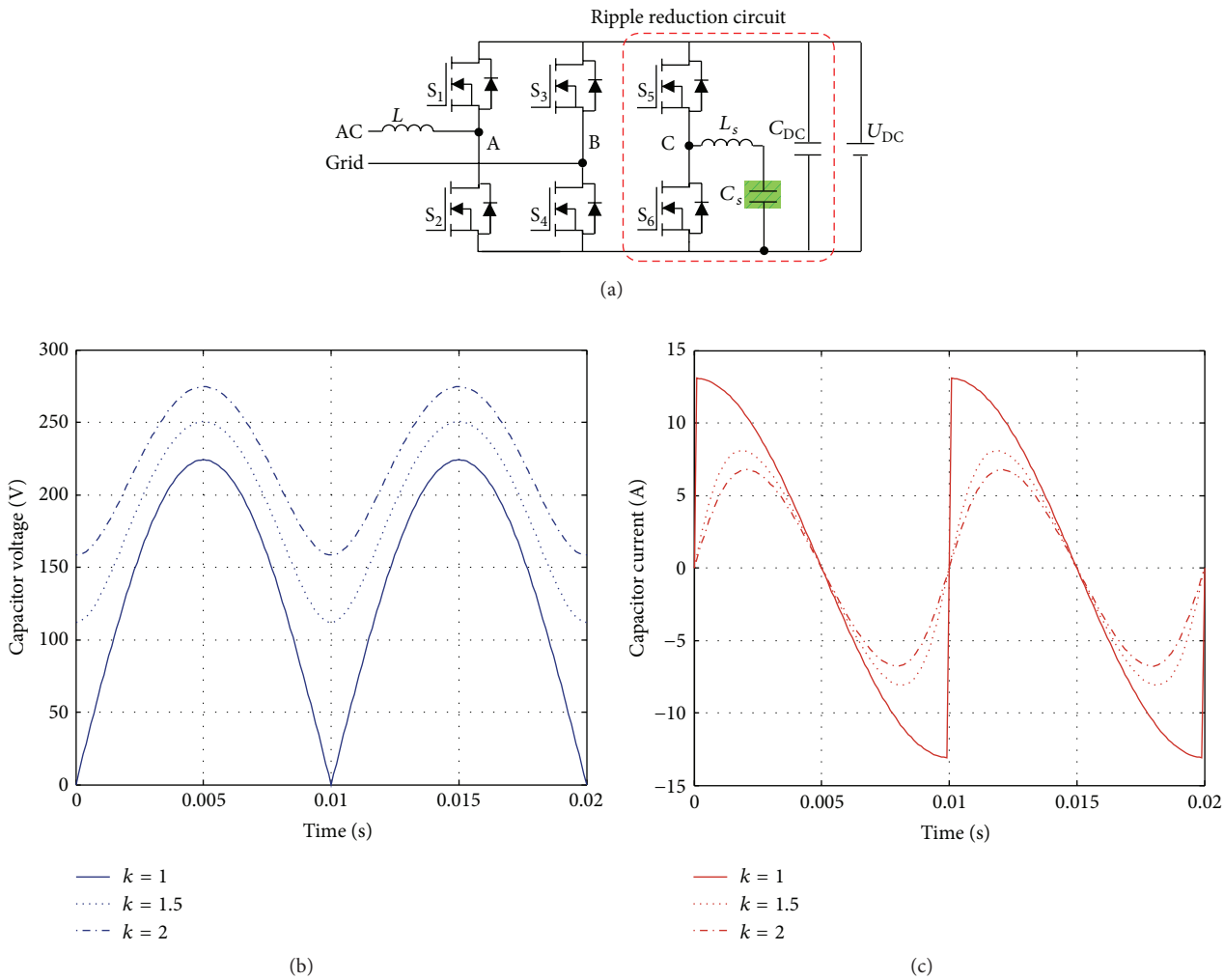

Figure 16: Capacitive storage method: (a) circuit configuration of capacitive storage method, (b) capacitive ripple voltage, and (c) capacitive ripple current.

results in less inductance. The trade-off between switching frequency and losses needs to be considered.

3.5. Capacitive Storage Method. A capacitor is used as the energy storage component is shown in Figure 16(a). One terminal of the storage capacitor is tied to the midpoint of the C-phase leg, while the other terminal is connected to the ground. A ripple energy storage component C_s with an energy transfer element L_s is used as an active ripple compensation circuit. The ripple power can be determined in

$$P_{\text{ripple}} = E_{\text{ripple}} * \omega = \sqrt{P_{\text{out}}^2 + \left[\left(\frac{2\omega L P_{\text{out}}^2}{U_s^2 \cos^2\varphi}\right) - P_{\text{out}}\left(\frac{\sin\varphi}{\cos\varphi}\right)\right]^2}. \quad (8)$$

The ripple energy storage capacitor voltage and current can be expressed as (9); Figures 16(b) and 16(c) show the ripple voltage and ripple current in power pulsating storage capacitor:

$$U_s = \sqrt{\frac{P_{\text{ripple}}\,(k - \cos(2\omega t))}{C_s \omega}}$$
$$i_s = \frac{P_{\text{ripple}} \sin(2\omega t)}{\sqrt{\left(P_{\text{ripple}}/C_s\omega\right)(k - \cos(2\omega t))}}, \quad (9)$$

where the coefficient k is the ripple energy storage margin coefficient defined by the maximum ripple energy and ripple energy stored in the capacitor and C_s is energy storage capacitance. The second-order ripple voltage and capacitive ripple current stored in the capacitor are plotted in Figures 17(a) and 17(b).

The minimum capacitance can be derived as

$$C_s = \frac{2P_{\text{ripple}}}{U_s^2 \omega}. \quad (10)$$

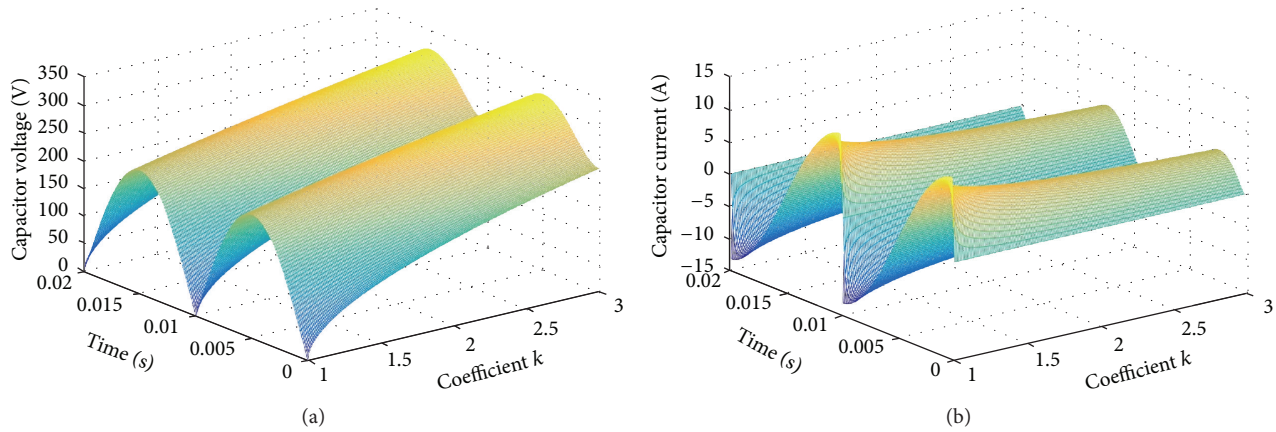

Figure 17: Second-order capacitive ripple voltage and capacitive ripple current: (a) capacitive ripple voltage and (b) capacitive ripple current.

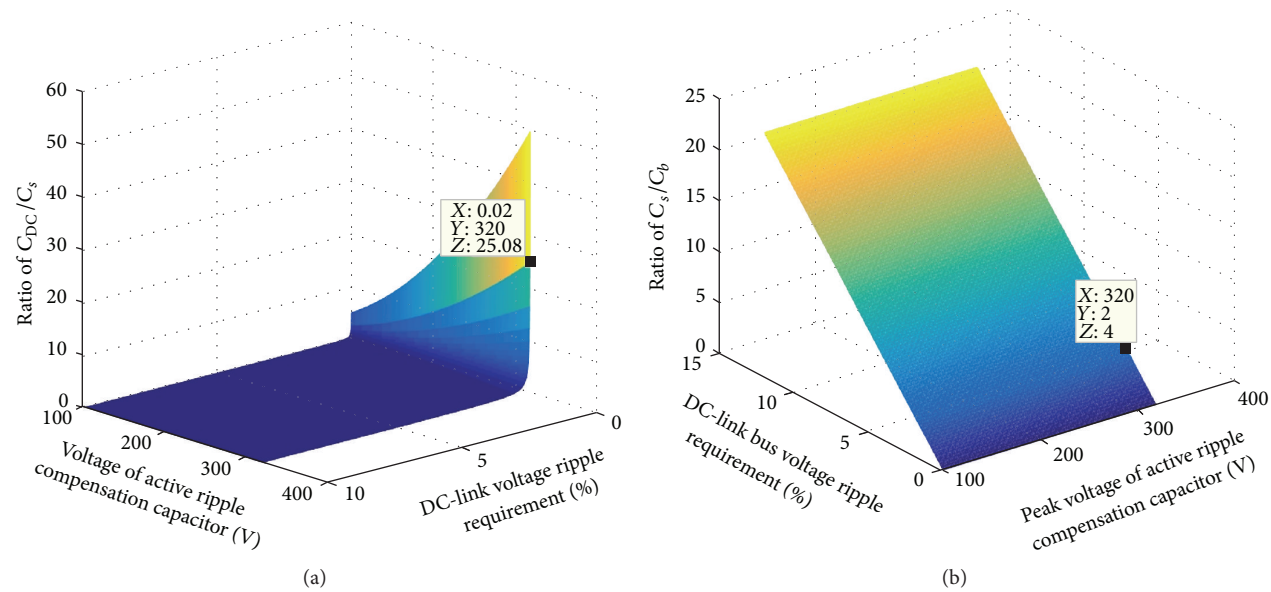

Figure 18: Comparison results between the DC-link capacitance and active ripple compensation methods: (a) capacitance comparison result and (b) current rating comparison result.

Equation (5) shows that the conventional design method calculates capacitance C_{DC} needed to filter the second-order harmonic in DC bus, while (10) shows that the active ripple storage capacitance C_s needed to meet the requirement of filtering the second-order ripple power. Figure 18(a) shows the capacitance comparison between the traditional method and the active method. It can be seen the active ripple method will decrease the capacitance 25.08 times compared with the conventional method within the 2% DC-link harmonic requirement. This indicates that the capacitance can decrease from 4.665 mF to 186 μF.

The active ripple compensation circuit works in discontinuous current mode (DCM) to meet the demand of maintaining ripple energy transfer inductance transfer 2ω power pulsating to the ripple energy storage capacitor completely. In DCM the current goes to zero during part of the switching cycle. In order to maintain DCM operation, the ripple energy transfer inductor selection limit can be expressed as (11):

$$L \leq \frac{T_{sw}}{2 * i_s} \frac{U_d U_s - U_s^2}{U_d}. \tag{11}$$

In addition, the active ripple compensation circuit requires one-phase leg which can share with three-phase inverter motor drive circuit, which has the maximum current rating limitation. The inductor selection limit based on the peak current requirement is expressed as

$$L \geq \frac{2 * \overline{i}_s * T_{sw}}{I_{peak}^2} \frac{U_d U_s - U_s^2}{U_d}. \tag{12}$$

The inductance is selected as 50 μH in the integrated charger system using (11) and (12). Table 4 shows the calculation results of inductive storage method and capacitive

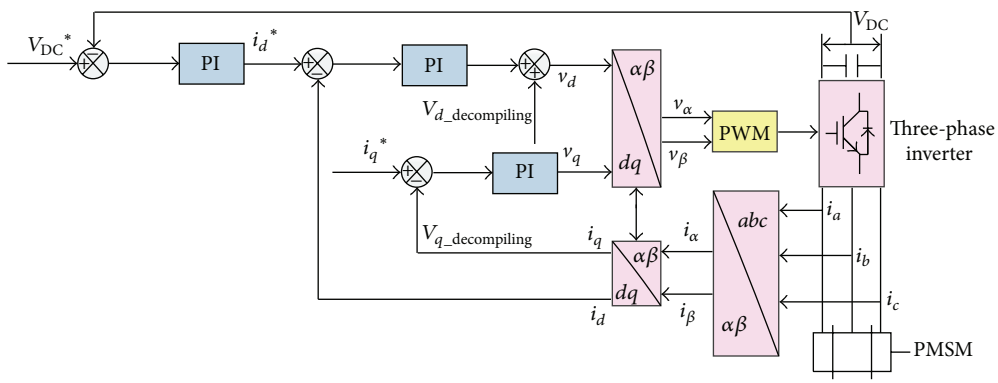

Figure 19: Control schematic figure for the circuit working as three-phase inverter.

Table 4: Comparison of inductive storage method and capacitive storage method.

Method	Capacitance	Inductance	Volume	Weight
Inductive storage method	—	68 mH	2762 cm^3	12.75 kg
Capacitive storage method	298 μF	50 μH	2895 cm^3	4 kg

storage method. Although the volume of the inductive storage devices can be smaller than the capacitive storage method, the weight of the inductor becomes much heavier than the capacitor. This demonstrates that capacitive storage method is superior to the inductive storage method in terms of power density of the charging circuit.

Although inductor is superior to capacitors from the viewpoint of ruggedness and reliability, inductor is inferior from the viewpoint of power density and weight. Power losses of inductor are also much higher than capacitor when working in high switching circuits [26–28]. Therefore, in this paper, an integrated charger topology employs a capacitor as the ripple energy storage element and an inductor as the ripple energy transfer component.

4. Control Design of Integrated Charger with Active Ripple Compensation

4.1. Motor Drive Control. In the motor drive mode, a closed-loop control schematic is illustrated in Figure 19. Both motor speed and current are regulated by applying PWM control to each phase switching device. The conventional PI controller including DC-link voltage control loop and current control loop are applied in three-phase inverter.

4.2. Battery Charging Control. The proposed active ripple energy absorbing method can generate the compensation ripple power successfully according to control capacitor voltage and current based on (9). The waveforms of capacitor reference voltage and reference current are essential issues to be considered besides ripple energy storage components. In Figure 16(b), the sharp turns at the bottom of the waveforms demonstrate large harmonic which is difficult to track for control strategy. It is possible to reduce the harmonic in the voltage reference and current reference by increasing the energy storage margin coefficient k which is set to 2 in this paper. The ripple current generated by H-bridge rectifier can be expressed as

$$i_{\text{ripple}} = (2D - 1)\, i_{\text{AC}}. \tag{13}$$

The reference compensation current is taken as minus ripple current for the active ripple compensation circuit, where D is duty cycle for H-bridge and i_{AC} is the AC-side current. The active ripple compensation circuit is controlled in bulk type and boost type to charge and discharge the ripple energy storage capacitor. The duty cycle for S_5 and S_6 can be derived as (14) and (15), respectively:

$$D_{\text{charging}} = \sqrt{\frac{2 \cdot i_{\text{ripple}} \cdot f_{\text{sw}}}{(U_d - U_s)/L}}, \tag{14}$$

$$D_{\text{discharging}} = \sqrt{\frac{2 \cdot i_{\text{ripple}} \cdot f_{\text{sw}} \cdot (U_d - U_s)/L}{(U_s/L)^2}}. \tag{15}$$

Based on the above discussion, the control block diagram is depicted in Figure 20. The upper part represents the control schematic for the PWM rectifier battery charging circuit and the lower part is the control strategy for the ripple reduction circuit. For PWM rectifier circuit, the DC-link voltage, DC-link current, and AC-side current are sensed to generate the gate drive signals for the main switches S_1, S_2, S_3, and S_4. In order to improve the performance of DC bus voltage, the AC-side voltage feedforward is adopted. A phase-locked loop (PLL) is constructed to track sinusoidal wave of the AC grid voltage as well. Via the proportional-integral (PI) controller, the command current i_{AC} is obtained to be equal to the command current i_{AC}^*. For ripple reduction circuit, the DC-link voltage and ripple energy storage capacitor voltage are sensed to generate the duty cycle for S_5 and S_6. According to the control method for C phase, if the compensation current is positive, the ripple reduction circuit is controlled to absorb the ripple energy from the DC-link charging the ripple compensation capacitor. Similar, if the compensation

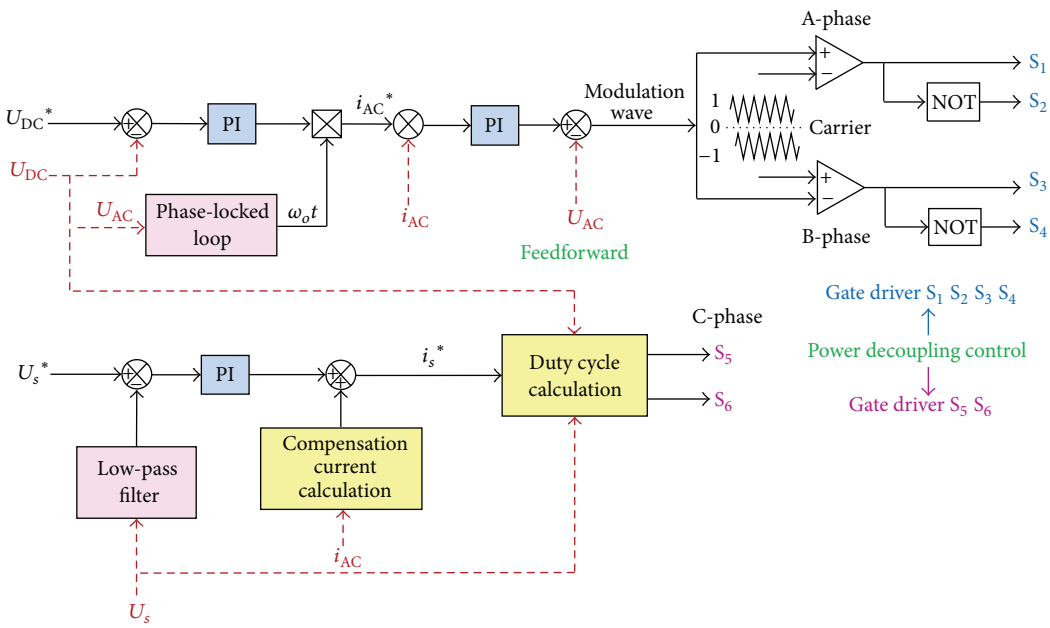

Figure 20: Control system for the integrated charger.

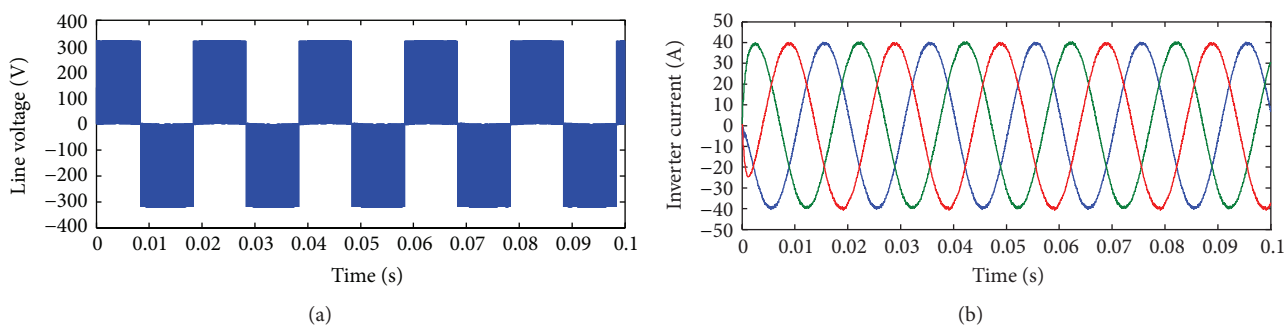

(a) (b)

Figure 21: Three-phase inverter simulation results: (a) the inverter output line voltage and (b) the inverter current.

current calculation result is negative, the ripple reduction circuit is controlled to release the ripple power into DC-link from ripple energy stored capacitor.

5. Simulation Results

The simulation parameters of the integrated charging converter are summarized in Tables 2 and 3. To evaluate the motor drive mode performance, a three-phase motor drive converter is modeled under PWM control in the simulation. Figure 21 presents the simulation results of motor drive.

Figure 22 presents the simulation results of battery charging without active ripple compensation circuit. Battery charging mode operation has been simulated under two conditions where the AC input voltage is lower than battery voltage, and DC input voltage is lower than battery voltage. When the input voltage is 230 V_{AC}, Figure 22(a) shows the output voltage. Figure 22(b) shows the maximum current ripple in grid side. The boost operation from the low-voltage bus to the battery has been simulated as shown in Figures 22(c)–22(f) with V_{batt} = 320 V and V_{lv} = 200 V.

Figures 23(a) and 23(b) show the integrated charger with active ripple compendation circuit main switch components duty cycle. It can be seen that the duty cycle for H-bridge PWM rectifier and the active ripple compensation circuit are decoupling. The most of the ripple power is stored in the DC bus capacitor without the active ripple compensation circuit. To meet the requirement of DC bus voltage ripple within 2% limit, a 4665 μF ripple energy storage capacitance is needed. A comparison of the DC bus voltage ripple performance without ripple reduction circuit and with active reduction circuit is provided in Figure 23. The simulation result in Figure 23(c) shows that the DC voltage ripple remains 74.64 V without active ripple compensation. When the C-phase leg is engaged, the 2ω ripple power is absorbed by the capacitor. A 298 μF capacitor and a 400 μF DC-link capacitor are used to be replaced by conventional large DC bus capacitor. The DC bus ripple voltage decreases to 4.6 V as shown in Figure 23(d).

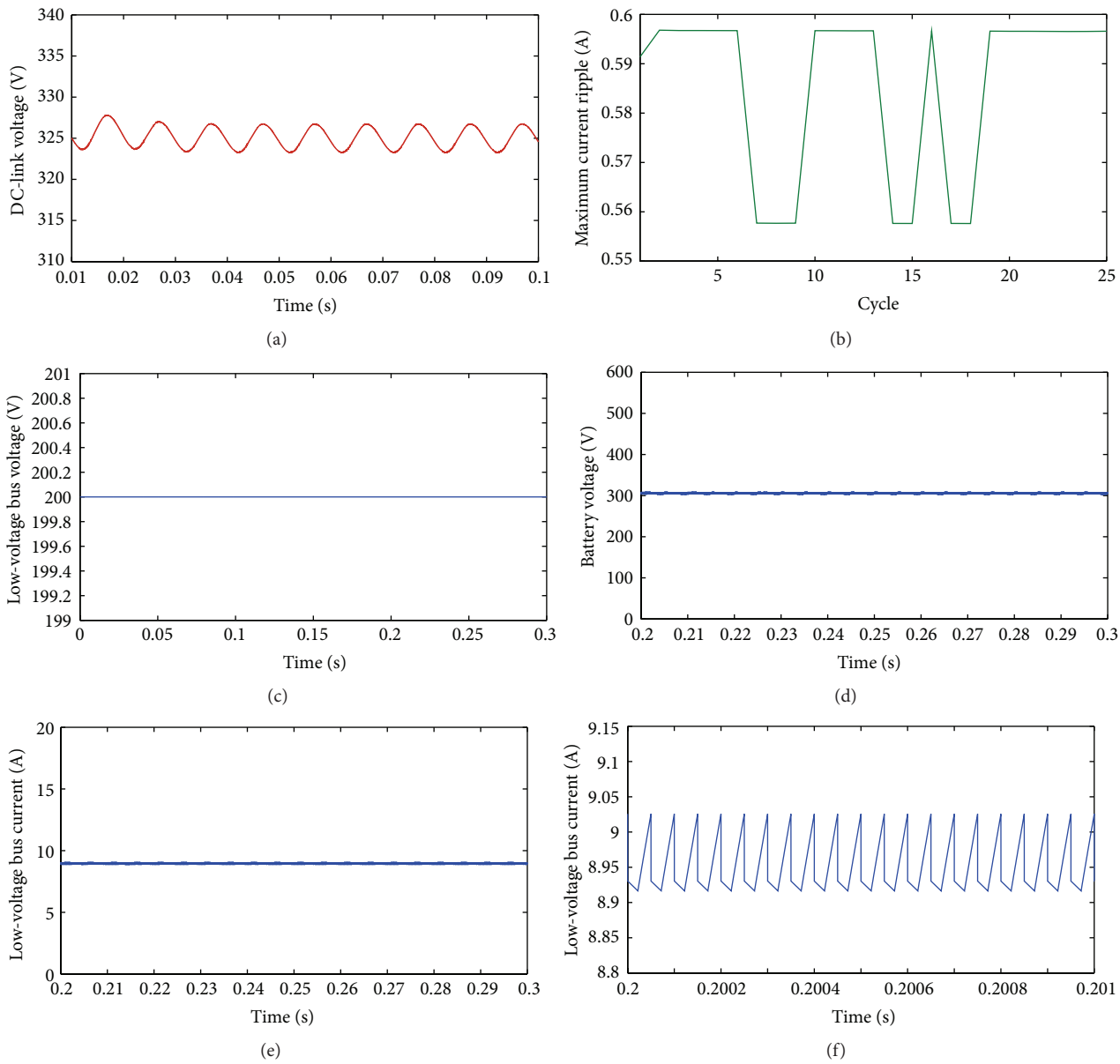

Figure 22: Simulation results for the AC/DC battery charging mode: (a) DC-link voltage and (b) AC-side maximum current ripple. Boost-type charging: (c) steady state for $V_{lv} = 200$ V, (d) steady state for $V_{batt} = 320$ V, (e) low-voltage bus current, and (f) zoom low-voltage bus current.

From Figures 23(e) and 23(f), it is shown that the DC ripple has been absorbed by the ripple power storage capacitor.

A comparison of the volume of the main components in the conventional method and the active ripple compensation method is illustrated in Figures 24(a) and 24(b). Using the active ripple compensation circuit to store the ripple energy is more effective. Conclusively, the whole integrated charger system volume decreases to 35% compared with the volume of the conventional method.

6. Power Losses and Thermal Analysis

In order to evaluate the thermal performance of the integrated charger with active ripple compensation converter topology, the power losses and device junction temperature are calculated and simulated. SiC-based devices meet the power electronics market demand for high performance 1200 V to 1700 V devices. SiC MOSFETs have unique capabilities such as lower switching loss, higher efficiency, and better temperature performance compared to Si-based devices when operating the same power rating which have essentially reached state-of-the-art limits in performance. In this paper, the performance of SiC MOSFET module from Cree CAS300M12BM2 (1.2 kV, 300 A) will be investigated. Figures 25(a) and 25(b) show the MOSFET and diode average losses of the motor drive mode and battery charging mode, which is derived by analytical models in [29]. Figure 25(c) shows the efficiency variation with various switching frequencies

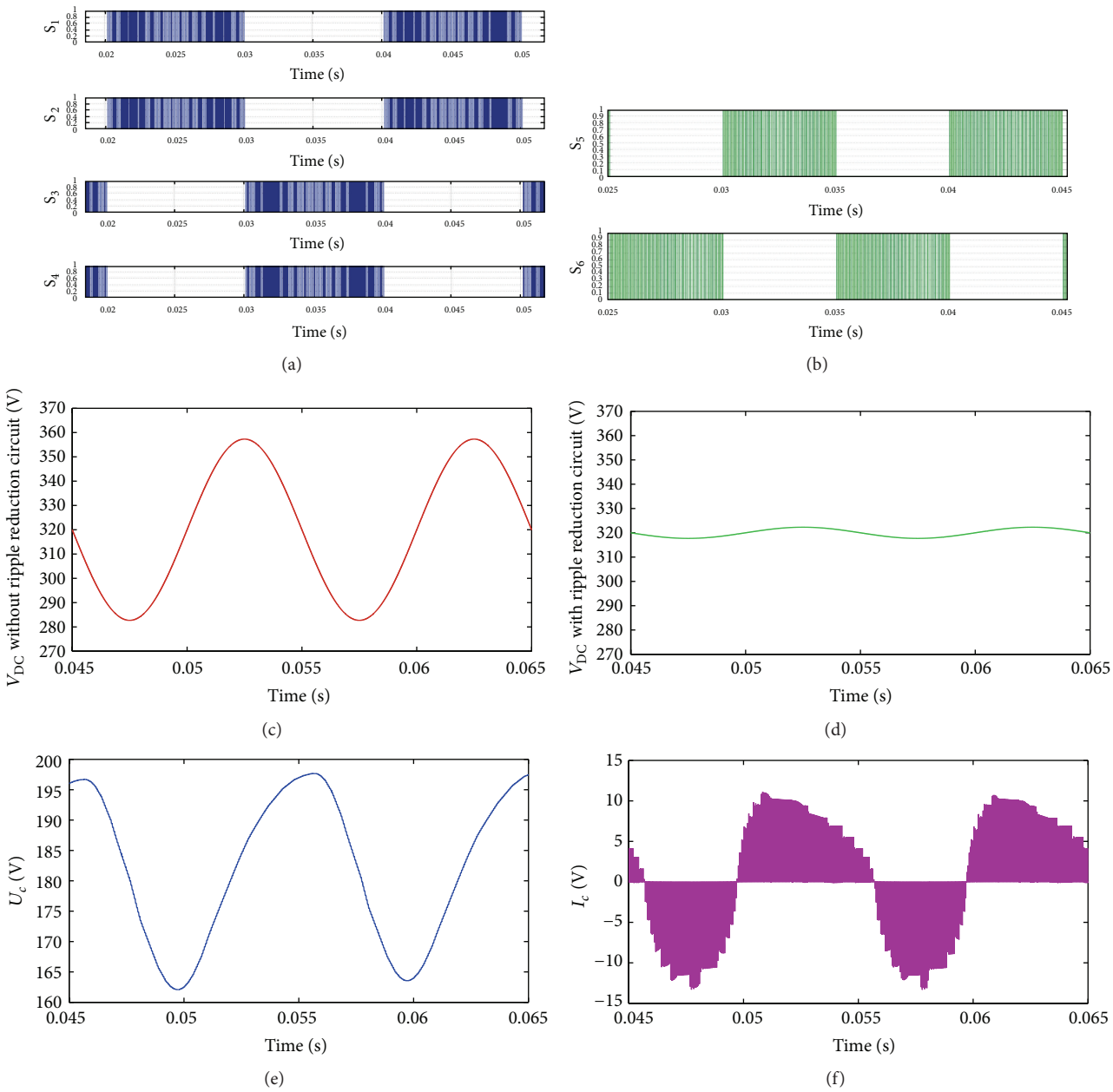

Figure 23: Duty cycle for the integrated charger: (a) H-bridge recitifier duty cycle and (b) active ripple compensation circuit duty cycle. Simulation results: (c) DC bus voltage without active ripple compensation circuit, (d) DC bus voltage with active ripple compensation circuit, (e) ripple power storage capacitor voltage, and (f) ripple power storage capacitor current.

for traction and charging operation [30–32]. In comparison to Si IGBT module from SK60GB128 (1.2 kV, 60 A) and SiC MOSFET (CAS300M12BM2) module, as expected, the SiC MOSFET shows a higher efficiency in a wide switching frequency range. With SiC MOSFET lower power losses and operation capability at higher switching frequency, integrated converter can operate up to 73 kHz switching frequency compared to 20 kHz using Si IGBT. The above results show that a clear advantage for SiC MOSFET is the candidate of choice to meet the demand of high power density and high efficiency in power converters application.

It is known that most of the failure mechanism such as bond-wire breakage is related to excessive temperature. Therefore, thermal behaviours management in power converter is essential to increase reliability performance [33]. Real-time junction temperature estimation requires calculation of the instantaneous losses in each MOSFET and diode device of the integrated charger. Therefore, the switching device conduction and switching losses every switching time cycle are calculated instantaneously [34]. The thermal model network includes thermal resistance and capacitance, which can transfer the power losses to the corresponding

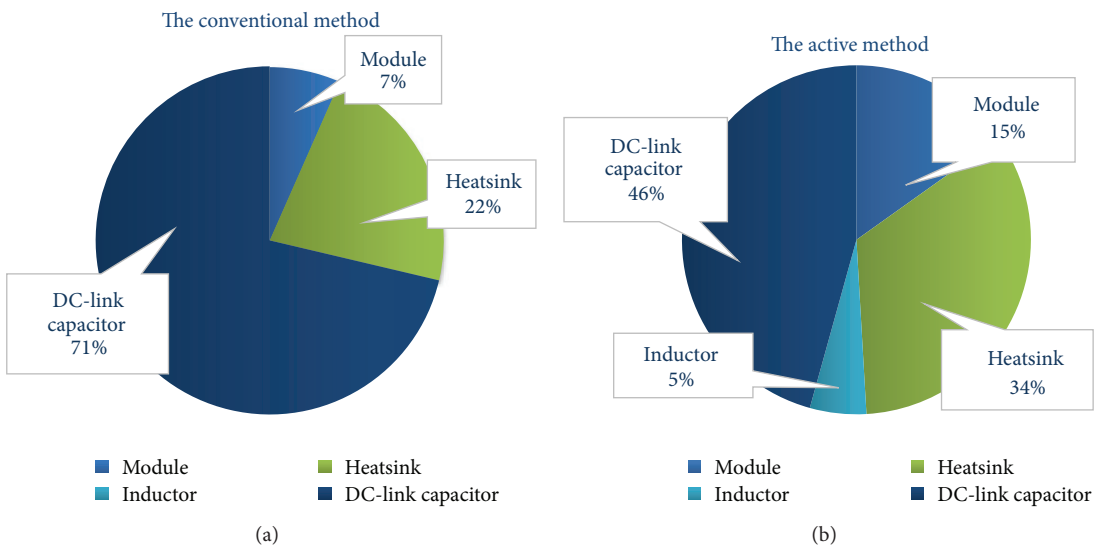

Figure 24: Power density: (a) conventional method main components volume comparison and (b) active method main components volume comparison.

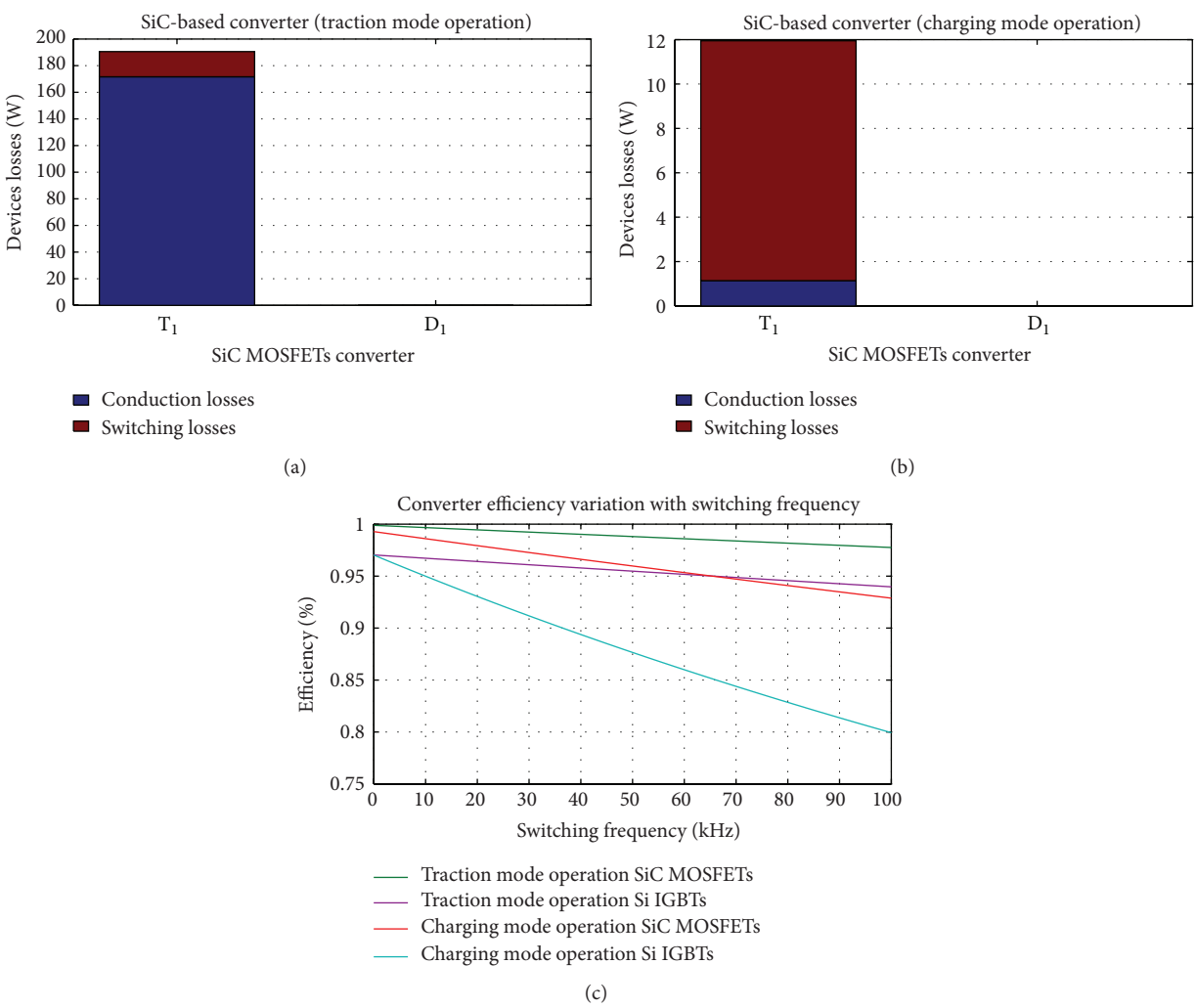

Figure 25: Calculation results: (a) traction mode operation, (b) charging mode operation, and (c) converter efficiency variation with switching frequency for SiC MOSFETs and Si IGBTs.

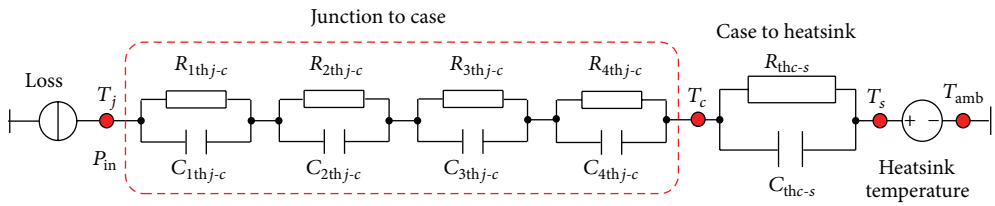

Figure 26: Thermal network (Foster model).

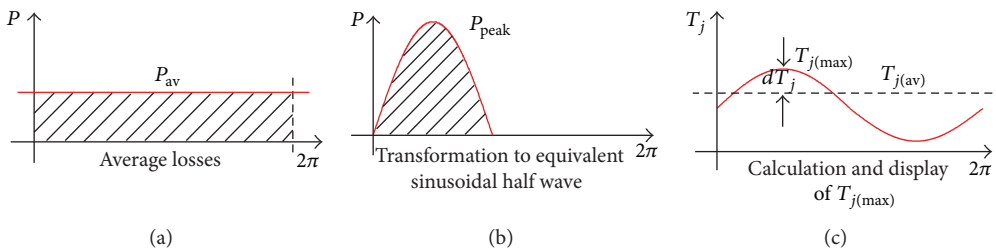

Figure 27: Calculation of the junction temperature fluctuation as a function of the converter output frequency. (a) Average losses. (b) Transformation to equivalent sinusoidal half wave. (c) Calculation and display of junction temperature value.

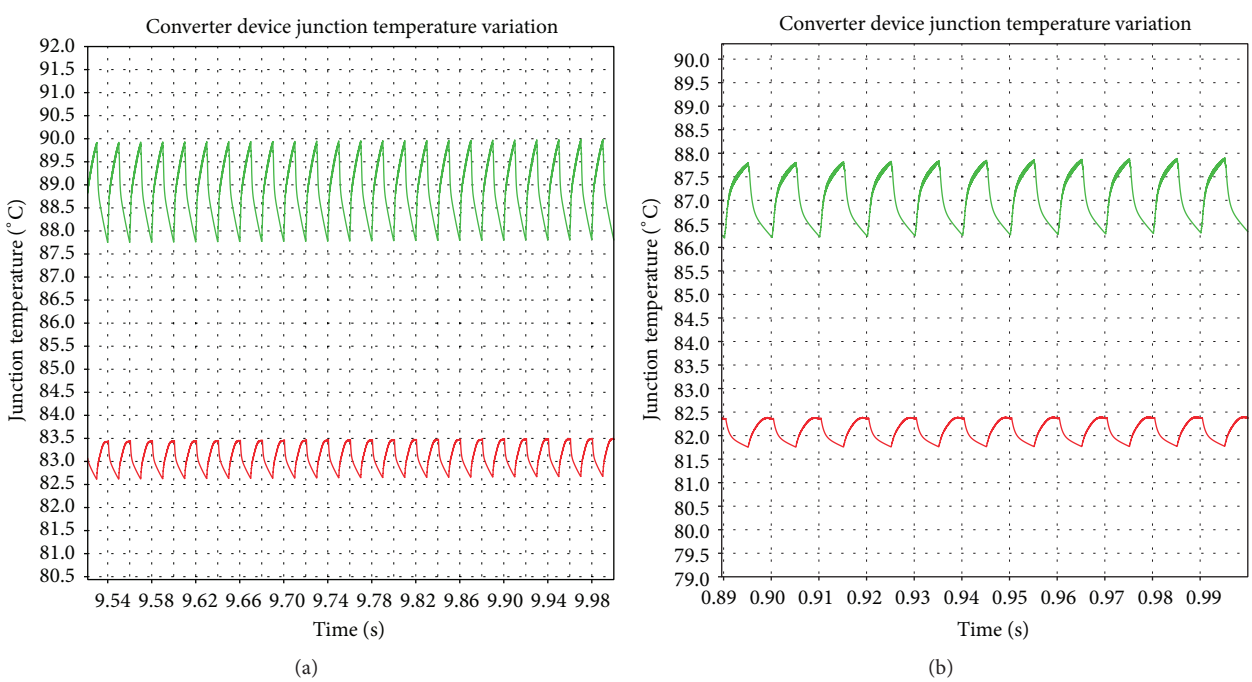

Figure 28: MOSFET/diode (battery charging mode) junction temperature variation: (a) single-phase circuit and (b) ripple energy storage circuit.

temperature in power devices. In the simulation, the heatsink temperature is assumed to be fixed at 80°C due to its large thermal time constant compared with converter devices [35]. As shown in Figure 26, the Foster thermal network is proposed which is used for junction temperature estimation. The parameters of the thermal network elements are given in the device datasheet [36].

The possible solution for junction temperature variation calculation is shown in Figure 27. A simulation based on transformation average losses to equivalent sinusoidal half wave method is used to evaluate the junction temperature variation of the battery charging mode. As shown in Figure 28(a), the single-phase SiC MOSFET junction temperature varies between 87.5°C and 90°C. The diode junction temperature varies between 82.5°C and 83.5°C. When the ripple energy storage circuit is applied, the SiC MOSFET temperature varies between 86.2°C and 87.7°C while the diode temperature varies between 81.8°C and 82.5°C. The junction temperature does not exceed the maximum allowable junction temperature 150°C.

7. Conclusion

In this paper, a concept of integrated charger with ripple reduction circuit for EV applications is proposed. The integrated converter reduces system cost, increases power density, and may lead to improved efficiency. The proposed integrated converter has been compared with existing topologies, and its advantages have been indicated. Additionally, exact system parameters, control strategy, power losses based on SiC MOSFET devices, efficiency, system power density, and thermal stress are discussed. In order to verify the proposed converter, the functionalities for different operating modes, for example, the boost for charging battery, buck for regenerative braking, and buck for motor drive, have been simulated. According to input/output-voltage-current conditions, the controller chooses the control schemes and proper operating modes. The DC bus low-frequency power pulsating generated from single-phase has been reduced efficiently by active ripple energy compensation circuit. To verity the practicality of the proposed converter for EV applications, an on-board experiment needs to be tested in the future.

Conflict of Interests

The authors declare that there is no conflict of interests regarding the publication of this paper.

Acknowledgments

The authors gratefully acknowledge the support from the Beijing Municipal Science and Technology Commission of China (Grant no. Z121100006612006). This paper is funded by International Graduate Exchange Program of Beijing Institute of Technology.

References

[1] F. Sun and R. Xiong, "A novel dual-scale cell state-of-charge estimation approach for series-connected battery pack used in electric vehicles," *Journal of Power Sources*, vol. 274, pp. 582–594, 2015.

[2] M. Yilmaz and P. T. Krein, "Review of battery charger topologies, charging power levels, and infrastructure for plug-in electric and hybrid vehicles," *IEEE Transactions on Power Electronics*, vol. 28, no. 5, pp. 2151–2169, 2013.

[3] S. Dieckerhoff, S. Bernet, and D. Krug, "Power loss-oriented evaluation of high voltage IGBTs and multilevel converters in transformerless traction applications," *IEEE Transactions on Power Electronics*, vol. 20, no. 6, pp. 1328–1336, 2005.

[4] K. L. Butler, M. Ehsani, and P. Kamath, "A matlab-based modeling and simulation package for electric and hybrid electric vehicle design," *IEEE Transactions on Vehicular Technology*, vol. 48, no. 6, pp. 1770–1778, 1999.

[5] S. Haghbin and M. Alakula, "Electrical apparatus comprising drive system and electrical machine with reconnectable stator winding," International Patent WO/2011/159241, 2011.

[6] A. G. Cocconi, "Combined motor drive and battery recharge system," US Patent 5 341 075, 1994.

[7] AC Propulsion, "AC propulsion EV drive system specifications," Technical Note, AC Propulsion, San Dimas, Calif, USA, 2008.

[8] W. E. Rippel, "Integrated traction inverter and battery charger apparatus," US Patent 4 920 475, 1990.

[9] W. E. Rippel and A. G. Cocconi, "Integrated motor drive and recharge system," US Patent 5 099 186, 1992.

[10] L. De-Sousa and B. Bouchez, "Combined electric device for powering and charging," International Patent WO 2010/057892 A1, 2010.

[11] L. De-Sousa and B. Bouchez, "Method and electric combined device for powering and charging with compensation means," Article ID 057893, International Patent WO 2010/057893 A1, 2010.

[12] S. Haghbin, M. Alakula, K. Khan et al., "An integrated charger for plug-in hybrid electric vehicles based on a special interior permanent magnet motor," in *Proceedings of the IEEE Vehicle Power and Propulsion Conference (VPPC '10)*, pp. 1–6, IEEE, Lille, France, September 2010.

[13] S. Lacroix, E. Laboure, and M. Hilairet, "An integrated fast battery charger for electric vehicle," in *Proceedings of the IEEE Vehicle Power and Propulsion Conference (VPPC '10)*, Lille, France, September 2010.

[14] D.-G. Woo, G.-Y. Choe, J.-S. Kim, B.-K. Lee, J. Hur, and G.-B. Kang, "Comparison of integrated battery chargers for plug-in hybrid electric vehicles: topology and control," in *Proceedings of the IEEE International Electric Machines and Drives Conference*, pp. 1294–1299, IEEE, Niagara Falls, Canada, May 2011.

[15] L. De Sousa, B. Silvestre, and B. Bouchez, "A combined multiphase electric drive and fast battery charger for electric vehicles," in *Proceedings of the IEEE Vehicle Power and Propulsion Conference (VPPC '10)*, pp. 1–6, Lille, France, September 2010.

[16] G. Pellegrino, E. Armando, and P. Guglielmi, "An integral battery charger with power factor correction for electric scooter," *IEEE Transactions on Power Electronics*, vol. 25, no. 3, pp. 751–759, 2010.

[17] H. Li, K. Zhang, H. Zhao, S. F. Fan, and J. Xiong, "Active power decoupling for high-power single-phase PWM rectifiers," *IEEE Transactions on Power Electronics*, vol. 28, no. 3, pp. 1308–1319, 2013.

[18] Y. Hayashi, K. Takao, T. Shimizu, and H. Ohashi, "High power density design methodology," in *Proceedings of the Power Conversion Conference—Nagoya (PCC '07)*, pp. 569–574, IEEE, Nagoya, Japan, April 2007.

[19] I. Laird, X. Yuan, and N. McNeill, "A holistic approach to optimise the power density of a silicon carbide (SiC) MOSFET based three-phase inverter," in *Proceedings of the IEEE 11th International Conference on Power Electronics and Drive Systems (PEDS '15)*, pp. 473–478, Sydney, Australia, June 2015.

[20] M. Yilmaz and P. T. Krein, "Review of battery charger topologies, charging power levels, and infrastructure for plug-in electric and hybrid vehicles," *IEEE Transactions on Power Electronics*, vol. 28, no. 5, pp. 2151–2169, 2013.

[21] Y. Hu, X. Song, W. Cao, and B. Ji, "New SR drive with integrated charging capacity for plug-in hybrid electric vehicles (PHEVs)," *IEEE Transactions on Industrial Electronics*, vol. 61, no. 10, pp. 5722–5731, 2014.

[22] Y. Hu, C. Gan, W. Cao, C. Li, and S. J. Finney, "Split converter-fed SRM drive for flexible charging in EV/HEV applications," *IEEE Transactions on Industrial Electronics*, vol. 62, no. 10, pp. 6085–6095, 2015.

[23] A. Y. Saber and G. K. Venayagamoorthy, "One million plug-in electric vehicles on the road by 2015," in *Proceedings of the 12th International IEEE Conference on Intelligent Transportation*

Systems (ITSC '09), pp. 141–147, IEEE, St. Louis, Mo, USA, October 2009.

[24] T. Shimizu, Y. Jin, and G. Kimura, "DC ripple current reduction on a single-phase PWM voltage-source rectifier," *IEEE Transactions on Industry Applications*, vol. 36, no. 5, pp. 1419–1429, 2000.

[25] X. Yuan and A. Lovett, "DC-link capacitance reduction in a high power medium voltage modular wind power converter," in *Proceedings of the 15th European Conference on Power Electronics and Applications (EPE '13)*, pp. 1–10, Lille, France, September 2013.

[26] R. Wang, F. Wang, D. Boroyevich et al., "A high power density single-phase PWM rectifier with active ripple energy storage," *IEEE Transactions on Power Electronics*, vol. 26, no. 5, pp. 1430–1443, 2011.

[27] H. Li, K. Zhang, H. Zhao, S. Fan, and J. Xiong, "Active power decoupling for high-power single-phase PWM rectifiers," *IEEE Transactions on Power Electronics*, vol. 28, no. 3, pp. 1308–1319, 2013.

[28] W. Qi, H. Wang, X. Tan, G. Wang, and K. D. T. Ngo, "A novel active power decoupling single-phase PWM rectifier topology," in *Proceedings of the 29th Annual IEEE Applied Power Electronics Conference and Exposition (APEC '14)*, pp. 89–95, IEEE, Fort Worth, Tex, USA, March 2014.

[29] X. Yuan, "Analytical averaged loss model of a three-level T-type converter," in *Proceedings of the 7th IET International Conference on Power Electronics, Machines and Drives*, pp. 1–6, April 2014.

[30] J. Liu and K. L. Wong, *Performance Evaluation of Hard-Switching Interleaved DC/DC Boost Converter with New Generation Silicon CarbideMOSFETs*, Cree, Durham, NC, USA.

[31] B. Callanan, "Application considerations for silicon carbide MOSFETs," Application Considerations for SiC MOSFET, January 2011.

[32] R. J. Callanan, A. Agarwal, A. Burk et al., "Recent progress in SiC DMOSFETs and JBS diodes at Cree," in *Proceedings of the 34th Annual Conference of IEEE Industrial Electronics (IECON '08)*, pp. 2885–2890, IEEE, Orlando, Fla, USA, November 2008.

[33] K. Ma, M. Liserre, and F. Blaabjerg, "Lifetime estimation for the power semiconductors considering mission profiles in wind power converter," in *Proceedings of the 5th Annual IEEE Energy Conversion Congress and Exhibition (ECCE '13)*, pp. 2962–2971, Denver, Colo, USA, September 2013.

[34] J. Lemmens, P. Vanassche, and J. Driesen, "Optimal control of traction motor drives under electrothermal constraints," *IEEE Journal of Emerging and Selected Topics in Power Electronics*, vol. 2, no. 2, pp. 249–263, 2014.

[35] X. Yuan and A. Lovett, "DC-link capacitance reduction in a high power medium voltage modular wind power converter," in *Proceedings of the 15th European Conference on Power Electronics and Applications (EPE '13)*, pp. 1–10, IEEE, Lille, France, September 2013.

[36] http://www.farnell.com/datasheets/1821845.pdf.

[37] SAE Electric Vehicle and Plug-in Hybrid Electric Vehicle Conductive Charge Coupler, SAE standard J1772, January 2010.